

Article

Synthesis and Characterization of Sr-Doped ZnSe Nanoparticles for Catalytic and Biological Activities

V. Beena^{1,*}, S. L. Rayar², S. Ajitha¹, Awais Ahmad^{3,*} , Munirah D. Albaqami⁴, Fatmah Ahmed Ali Alsabar⁴ and Mika Sillanpää^{5,6,7,8,9,*} 

¹ Department of Physics, Nanjil Catholic College of Arts and Science, Manonmaniam Sundaranar University, Kanyakumari 629153, India; ajithaphyholo@gmail.com

² Dept of Physics, St. Judes College, Kanyakumari 629176, India; drslrayar@gmail.com

³ Departamento de Quimica Organica, Universidad de Cordoba, Edificio Marie Curie (C-3), Ctra Nnal IV-A, Km 396, E14014 Cordoba, Spain

⁴ Chemistry Department, College of Science, King Saud University, Riyadh 11451, Saudi Arabia; muneerad@ksu.edu.sa (M.D.A.); 439203369@student.ksu.edu.sa (F.A.A.A.)

⁵ Department of Civil and Environmental Engineering, Florida International University, Miami, FL 33027, USA

⁶ School of Resources and Environment, University of Electronic Science and Technology of China (UESTC), NO. 2006, Xiyuan Ave., West High-Tech Zone, Chengdu 611731, China

⁷ Faculty of Science and Technology, School of Applied Physics, University Kebangsaan Malaysia, Bangi 43600, Malaysia

⁸ International Research Centre of Nanotechnology for Himalayan Sustainability (IRCNHS), Shoolini University, Solan 173212, India

⁹ Department of Biological and Chemical Engineering, Aarhus University, Nørrebrogade 44, 8000 Aarhus C, Denmark

* Correspondence: drbeenaphysics@gmail.com (V.B.); awaisahmed@gcuf.edu.pk (A.A.); mikaesillanpaa@gmail.com (M.S.)



Citation: Beena, V.; Rayar, S.L.; Ajitha, S.; Ahmad, A.; Albaqami, M.D.; Alsabar, F.A.A.; Sillanpää, M. Synthesis and Characterization of Sr-Doped ZnSe Nanoparticles for Catalytic and Biological Activities. *Water* **2021**, *13*, 2189. <https://doi.org/10.3390/w13162189>

Academic Editor: Antonio Zuorro

Received: 7 July 2021

Accepted: 4 August 2021

Published: 11 August 2021

Publisher's Note: MDPI stays neutral with regard to jurisdictional claims in published maps and institutional affiliations.



Copyright: © 2021 by the authors. Licensee MDPI, Basel, Switzerland. This article is an open access article distributed under the terms and conditions of the Creative Commons Attribution (CC BY) license (<https://creativecommons.org/licenses/by/4.0/>).

Abstract: The development of cost-effective and ecofriendly approaches toward water purification and antibacterial activity is a hot research topic in this era. Purposely, strontium-doped zinc selenide (Sr-doped ZnSe) nanoparticles, with different molar ratios of Sr²⁺ cations (0.01, 0.05, and 0.1), were prepared via the co-precipitation method, in which sodium borohydride (NaBH₄) and 2-mercaptoethanol were employed as reducing and stabilizing agents, respectively. The ZnSe cubic structure expanded by Sr²⁺ cations was indicated by X-ray diffraction (XRD) analysis. The absorption of the chemical compounds on the surface was observed via Fourier transform infrared (FT-IR) spectroscopy. The optical orientation was measured by ultraviolet–visible diffused reflectance spectroscopy (UV-DRS) analysis. The surface area, morphology, and elemental purity were analyzed using field emission scanning electron microscopy (FE-SEM), high-resolution transmission electron microscopy (HR-TEM), and energy-dispersive spectroscopy (EDS) analyses. The oxidation state and valency of the synthesized nanoparticles were analyzed using X-ray photoelectron spectroscopy (XPS). Sr-doped ZnSe nanoparticles were investigated for photocatalytic degradation of methyl orange (MO), and their antibacterial potential was investigated against different bacterial strains. The antibacterial activity examined against *Staphylococcus aureus* and *Escherichia coli* implied the excellent biological activity of the nanoparticles. Moreover, the Sr-doped ZnSe nanoparticles were evaluated by the successful degradation of methyl orange under visible light irradiation. Therefore, Sr-doped ZnSe nanoparticles have tremendous potential in biological and water remediation fields.

Keywords: Sr-doped ZnSe nanoparticles; co-precipitation; antibacterial; dye degradation

1. Introduction

Water contamination is a vital environmental issue that exhibits catastrophic consequences for the world [1]. The largest water pollution sources are organic pollutants, dyes, and inorganic heavy metals [2,3]. The industries that are declared as the main sources

of these water pollutants include the pharmaceutical, textile, dyeing, and metallurgical industries, among others. [4,5]. Dye waste from various industries, including some textiles, leather, pharmaceuticals, paper mills, and so on, is one of the primary pollutants of the water, posing a serious threat to individuals and the environment [6,7]. Purposely, various chemical, physical, and biological methods have been used for wastewater treatment, which includes filtration, advanced oxidation, flocculation and coagulation, catalysis, photo and chemical degradation, and adsorption [8,9]. In this way, photocatalysis provides a low-cost and reliable treatment for water purification [10–12]. As a consequence, scientific research is focused on the development of new eco-friendly and cost-effective materials for the elimination of harmful contaminants from wastewater streams. Because of their intriguing chemical and physical characteristics, semiconductor nanostructures have shown some efficiency regarding the photocatalytic removal of industrial effluents [13,14]. Numerous semiconductors have also been developed for the treatment of contaminated waters. Metal oxides, such as TiO_2 [15], ZnO [16], SnO_2 [17], as well as group II–VI compounds, such as CdS [18], CdTe [19], HgS [20], and ZnS [21], are among the most frequently employed photocatalysts.

In addition, bacteria present a serious health threat, requiring the development of novel and more efficient antibacterial therapeutics [10,22]. Recently, nanomaterials exhibiting potential antibacterial activity have been observed as novel materials in the treatment of bacterial infections [23,24]. Accordingly, scientists are now focused on nano-bioscience because of its specific antibacterial potential. AgO and CuO [25], Sr-Ag [26], Cu [27], ZnO [28], CdS [29], and many more compounds are reported as efficient antibacterial agents in different biological activities.

Among these materials, ZnSe is a promising semiconductor material with appropriate physical and chemical properties, enabling it to be an ideal material for a wide range of applications [30,31]. ZnSe nanoparticles have been used in a vast array of laser and optical devices. They possess a wide bandgap and transmittance range, as well as a high luminescence efficiency, low absorption coefficient, and excellent infrared transparency [32]. The improved photocatalytic capabilities of doped ZnS NPs prepared through the hydrothermal route make them attractive candidates for the degradation of different organic dyes [33]. However, the catalytic efficiency and biological activity of ZnSe nanoparticles can be enhanced by the incorporation of various dopants, such as Er [34], Mn [35,36], Cd [37], Mo [38], etc. Physicochemical parameters, e.g., temperature, capping, reducing agents, etc., exert a strong impact on the shape and size of nanoparticles, which makes them a potential candidate for different applications, such as catalysis, sensing, and environmental remediations. Increasing the temperature yields smaller particles and a narrow size distribution [39,40]. In addition, capping agents such as surfactants, polymers, etc. affect the morphology of nanoparticles [41]. A decrease in particle size has also been observed with an increase in pH [41]. According to this research, Sr-doped ZnSe materials may reveal catalytic activity against dye molecules, and their lower valency induces the release of ions, which can control cell multiplication.

The present work investigated the degradation of methyl orange dye and action against noxious bacteria by Sr-doped ZnSe nanoparticles. The Sr-doped ZnSe nanoparticles were synthesized via the co-precipitation method, and different characterization techniques, i.e., XRD, FTIR, UV-DRS, FE-SEM, EDX, HR-TEM, and XPS, were used to analyze their structural, morphological, and catalytic properties.

2. Materials and Methods

2.1. Chemicals and Reagents

Strontium nitrate ($\text{Sr}(\text{NO}_3)_2$), zinc acetate dihydrate ($\text{C}_4\text{H}_6\text{O}_4\text{Zn} \cdot 2\text{H}_2\text{O}$), 2-mercaptoethanol ($\text{C}_2\text{H}_6\text{OS}$), sodium borohydride (NaBH_4), methyl orange dye ($\text{C}_{14}\text{H}_{14}\text{N}_3\text{NaO}_3\text{S}$), and sodium hydroxide (NaOH) were used as chemicals in the synthesis of nanoparticles. All the chemicals were bought from HiMedia, India (99% purity). The chemicals were used

without any further processing. Double distilled water was used as a solvent for solution preparation and washing.

2.2. Synthesis of Sr-Doped Znse Nanoparticles

Sr-doped ZnSe nanoparticles, synthesized following a co-precipitation method, were obtained using a two-step process [42]. The first step was mixing Sr^{2+} at different molar concentrations (0.01, 0.05, and 0.1) and 0.5 M zinc acetate with 2-mercaptoethanol using a magnetic stirrer. 2-Mercaptoethanol acted as a capping agent that provided steric stabilization to the synthesized nanoparticles [43,44]. At the same time, 0.5 M metal selenium was dissolved by an NaBH_4 solution to attain the sodium hydrogen selenide (NaHSe) solution. The dissolved solution was mixed with strontium and zinc, the combined solution was subjected to heating at $100\text{ }^\circ\text{C}$, and the pH was maintained at 10 which was controlled by using NaOH solution. The annealing temperature affected the size and morphology of nanoparticles.

The second step was a time-consuming process. The mixed solution reactions were carried out within 24 h. The Sr^{2+} doped ZnSe nanoparticles were obtained in the form of a precipitate. The precipitate was processed by double distilled water and ethanol to remove the impurities. The precipitate was kept in the oven at $80\text{ }^\circ\text{C}$ for 48 h, followed by heating at $200\text{ }^\circ\text{C}$. The synthesis scheme is demonstrated in Figure 1.

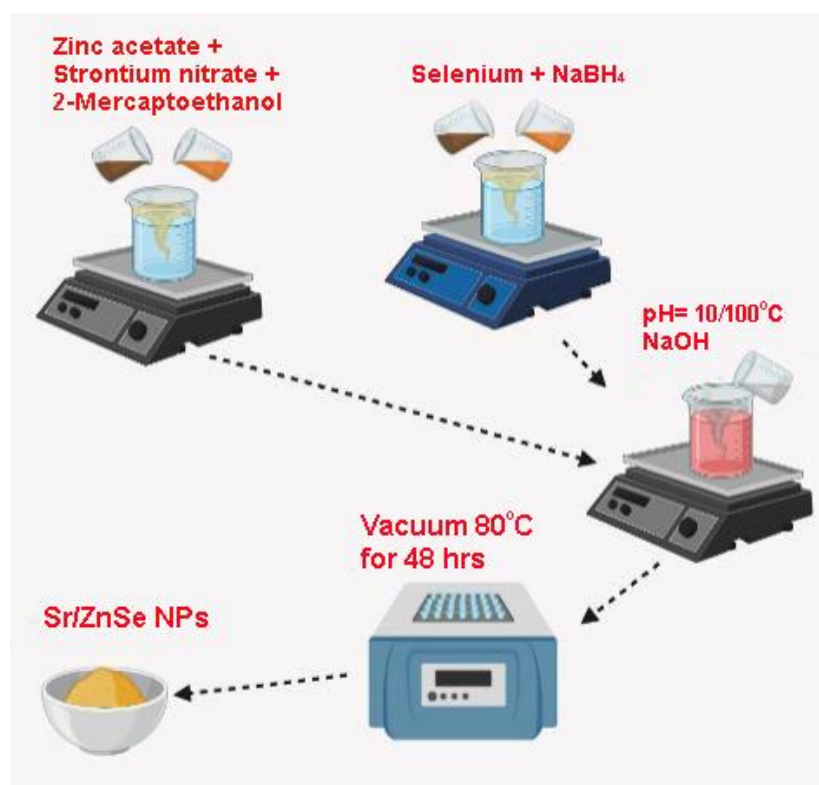


Figure 1. Synthesis process of the Sr-doped ZnSe nanoparticles.

2.3. Characterization

The structural nature and crystalline phase were identified from XRD analysis (PANalytical X-ray diffractometer) (JDX-3532, JEOL, Tokyo, Japan), with $\text{Cu-K}\alpha$ wavelength and 2θ ranging from 10° to 80° . The surface variations, particle size, and elemental analysis were recorded from FESEM with EDX (JSM-5910, JEOL, Tokyo, Japan) and HRTEM (JEOL-2100). The absorbed molecules were analyzed by using an FTIR spectrometer (Perkin Elmer), while the optical behaviors were calibrated by UV-Vis DRS (UV Shimadzu-2700). The binding between the orbitals and their energy was captured by the XPS technique (XPS, PHI 500, California, USA).

2.4. Antibacterial Activity

The Sr²⁺ doped ZnSe nanoparticles (0.1 M) were investigated for the antibacterial activity against *Staphylococcus aureus* (*S. aureus*) and *Escherichia coli* (*E. coli*). The disc diffusion method was used to evaluate antibacterial activity. The bacteria was evolved in Mueller Hinton broth (24 h). The evolved bacteria were separated and streaked on sterilized Petri plates (100 µL × 10⁻⁷ cm CFU broth conditions). The 6 mm disc was located by three different diluted concentrations of Sr-doped ZnSe nanoparticles (25 µL, 50 µL, and 100 µL). The nanoparticle-conceived discs were kept in an incubator for 24 h at 37 °C. The incubated discs revealed information about Sr-doped ZnSe nanoparticles. The formed zone from the disc denoted the antibacterial activity of the Sr-doped ZnSe nanoparticles.

2.5. Photocatalytic Activity

The ZnSe- and Sr- modified ZnSe nanoparticles were found to be highly responsive to visible light, acting as photocatalysts in a robust way to achieve the elimination of pollutants from the environment. MO was used as a model pollutant for the dye degradation study at a concentration of 10 ppm (100 mL). The Sr-doped ZnSe nanoparticles were used as catalysts in an amount of 10 mg at three different concentrations of Sr-doped ZnSe nanoparticles. The dye and catalyst were mixed using a magnetic stirrer in the dark for 30 min to achieve an absorption–desorption equilibrium condition. The mixed solution was stirred, and visible light was irradiated by the combined solution. After an interval of 15 min, the samples were taken out and centrifuged at 5000 rpm to remove the catalyst from the dye solution. The obtained samples were measured by UV–Vis at 465 nm [45]. The dye degradation efficiency “η” (%) was calculated using Equation (1) [7].

$$\eta \% = \frac{C_0 - C_t}{C_0} \times 100 \quad (1)$$

Here, C₀ corresponds to the initial absorbance value of the dye molecules, and C_t denotes the irradiate absorbance value of the dye molecules.

3. Results and Discussion

3.1. XRD Analysis

The structural crystallinity, size, and shape were analyzed using XRD. The Sr-doped ZnSe nanoparticle XRD pattern displayed in Figure 2 shows the crystallographic structure and phase nature of the samples. The Sr²⁺ cations were doped into interstitials of the ZnSe nanostructure. Therefore, was is no extra phase observed, but the FWHM was slightly increased; this increasing FWHM denotes the increase of crystallite size. The raw ZnSe nanoparticle crystallite size was 12 nm, and the substitution of Sr²⁺ increased the size of the samples. The obtained peaks suggest that the sample was in crystalline nature, and their 2θ values were 27.3°, 45.3°, 53.7°, 66.03°, and 72.7°, corresponding to the plane values of (1 1 1), (2 2 0), (3 1 1), (4 0 0), and (2 0 3), respectively. The average crystallite sizes were calculated using the Sherrer formula expressed in Equation (2) [46].

$$D = \frac{k\lambda}{\beta \cos \theta} \quad (2)$$

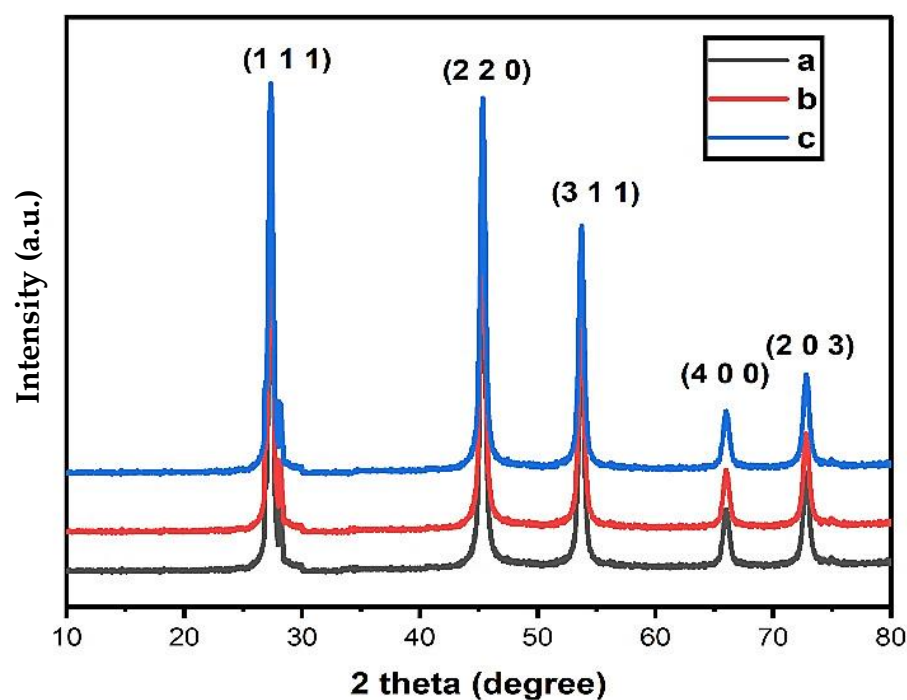


Figure 2. X-ray diffraction patterns of Sr (0.01 (a), 0.05 (b), and 0.1 (c))-doped ZnSe nanoparticles.

Here, D signifies the average crystallite size of the nanoparticles; k denotes the constant shape factor, which is 0.9; λ specifies the X-ray wavelength; β relates to the full width at half maximum (FWHM), and θ expresses Bragg's angle.

The calculated D values were 21, 26, and 35 nm for the 0.01, 0.05, and 0.1 molar ratios of Sr, respectively. The raw ZnSe nanoparticle size was low compared with Sr-doped ZnSe nanoparticles [45]. The Sr^{2+} doping was doped into the interatomic gaps of the ZnSe nanoparticles. Particularly, sample C showed high-intensity peaks, which indicated good substitution of Sr into the ZnSe nanoparticles. In the Sr lattice fully doped with the ZnSe setup, the peaks demonstrate the doping as well as quantitative phase of the Sr-doped ZnSe nanoparticles. Therefore, there was no extra peak in the XRD spectrum, but the sizes increased with the addition of Sr^{2+} cations. The obtained peaks were well coordinated with the std. JCPDS card no. of 88-2345 of the ZnSe cubic system [47]. Sample C (0.1) had high accordance and better crystallinity than samples B (0.05) and A (0.01).

3.2. FTIR Analysis

The functional groups of the synthesized nanoparticles were observed in the FTIR spectrum and ranged from 4000 to 400 cm^{-1} . The Sr-doped ZnSe nanoparticles in various concentrations of FTIR spectra are depicted in Figure 3. The low concentration of Sr^{2+} cations into the ZnSe nanoparticles exhibited strong peaks of 1575 cm^{-1} , 1359 cm^{-1} , 1249 cm^{-1} , and 1021 cm^{-1} , responsible for the OH-bending, C-O stretching, C-H bending, respectively. The increase in Sr^{2+} could shift the peaks toward the lower wavelength side. This peak-shifting indicates the substitution of Sr^{2+} cations to the ZnSe nanoparticles. The characteristic peaks of 725 and 486 cm^{-1} denote the formation of ZnSe nanoparticles in the Zn-Se stretching vibration.

The addition of Sr resulted in extra elemental peaks in the FTIR spectrum. Peaks of 800–400 cm^{-1} corresponded to Sr^{2+} cations in the Zn-Se stretching vibration. The Sr reduction to the ZnSe nanoparticles was indicated by the decrease of the O-H stretching and the appearance of new peaks from the pure ZnSe nanoparticles. The Zn^{2+} and Sr reduction and stabilization were confirmed, and Sr^{2+} substitutions were also confirmed by the peaks at 1000–400 cm^{-1} . The FTIR spectra are evidence of the reduction of Sr and Zn, and Se stabilized to the Sr-doped ZnSe nanoparticles was identified [48–51].

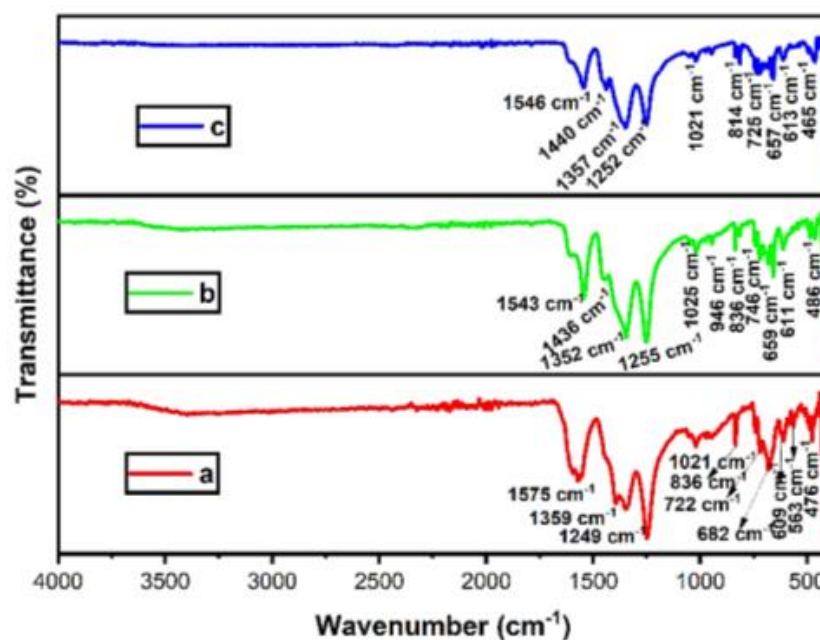


Figure 3. FTIR spectrum of Sr (0.01 (a), 0.05 (b), and 0.1 (c))-doped ZnSe nanoparticles.

3.3. UV-DRS Analysis

The data for the optical and electronic transition of the synthesized samples were collected from UV-DRS studies. The UV-DRS absorbance spectrum of Sr-doped ZnSe nanoparticles, illustrated in Figure 4a,b, determined the absorbance of Sr-doped ZnSe nanoparticles. The observed peaks for doped nanoparticles lay in the visible region, but the absorption for undoped ZnSe nanoparticles lay in the UV region. Such region transformation referred to the transition between the electrons. The Sr 3d orbitals electrons moved to the confined ZnSe arrangement. The ZnSe (Zn 2p and Se 3d) nanoparticle surfaces were modified with the Sr atoms. Therefore, the optical absorption moved from the UV region to the visible region [52].

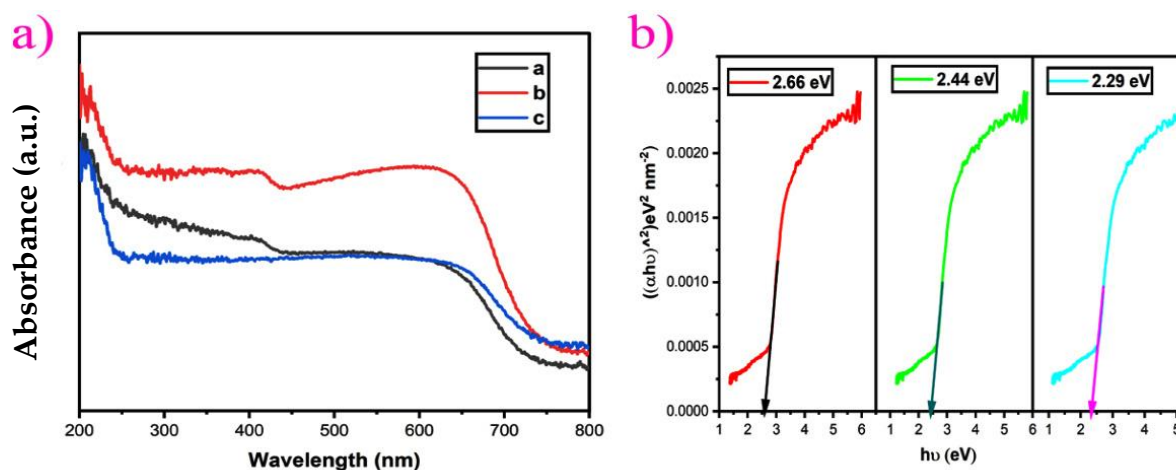


Figure 4. (a) UV-Vis DRS spectra and (b) bandgap spectrum of the Sr [0.01 (a), 0.05 (b) and 0.1 (c)] doped ZnSe nanoparticles.

Moreover, Tauc plots were used to measure the bandgap of the synthesized materials. The Sr distribution over the ZnSe nanoparticles decreased the gap between the electrons and the holes of the materials. Their modification increased the cavity to the surface. The bandgap values were 2.66 eV, 2.44 eV, and 2.29 eV for samples A, B, and c, respectively. The obtained bandgap values indicated the formation of the nanoparticles [53]. The nanoparticles with low bandgap values produced high quantum fields, which is a major

characteristic responsible for the UV–Vis region photocatalyst. The low bandgap and low crystallite size produced enhanced catalytic activity toward the dye molecules.

3.4. FE-SEM Analysis

The surface morphology of the synthesized Sr-doped ZnSe nanoparticles was analyzed via FE-SEM images, as shown in Figure 5a–c. The surface of the synthesized nanoparticles varied with the addition of dopant content in the ZnSe. The surfaces of undoped ZnSe nanoparticles resembled spherical-shaped particles, but their surfaces were engaged by the incorporation of Sr²⁺ ions [54]. Figure 5a shows the nanosheet-like shape at a low concentration of Sr. The Sr increase induced the structure nanosheet to nanoflower in Figure 5b,c. The sample was nanoflower-like, which exhibited a large surface area compared with pure ZnSe nanoparticles. The high surface area promoted enhanced catalytic and bactericidal activity.

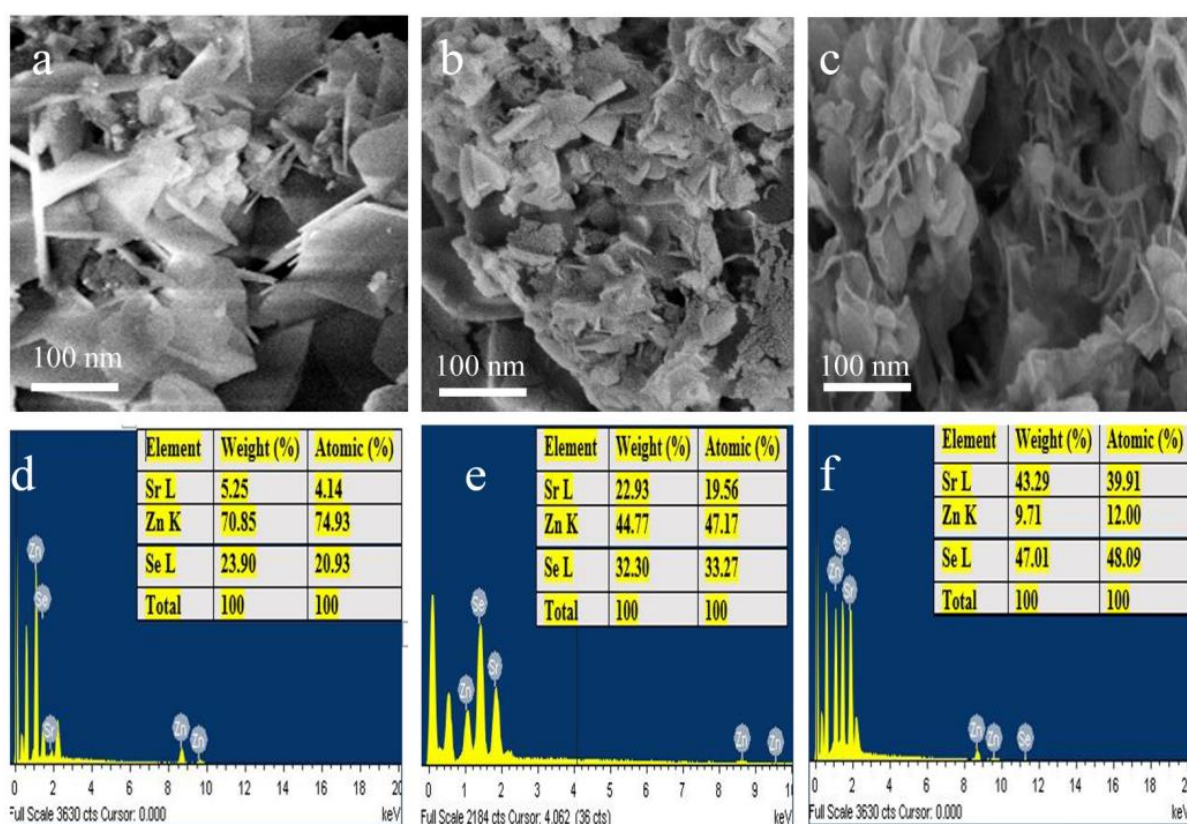


Figure 5. (a–c) FE-SEM images and (d–f) EDS spectra of Sr (0.01, 0.05, and 0.1)-doped ZnSe nanoparticles.

3.5. EDS Analysis

The elemental composition of the synthesized samples was evaluated by the EDS spectra displayed in Figure 5d–f. The EDS analysis confirmed the existence of metal in the synthesized sample. The zinc, selenium, and strontium peaks represent optical absorption of the energy of different values. The elements atomic and weight percentage of the synthesized samples are tabulated in Figure 5d–f. The higher amount of Sr²⁺ decreased the zinc distribution and increased the selenium distribution to the surface. The higher Sr content produced a larger area of optical absorption at the surface.

3.6. HR-TEM Analysis

The surface morphology, shape, and particle size were evaluated by HR-TEM analysis. Figure 6 shows the morphology of the synthesized Sr-doped ZnSe nanoparticles. The Sr²⁺ penetrated the ZnSe lattice. The undoped ZnSe nanoparticles exhibited a spherical shape,

while the dopants of Sr^{2+} reformed the spherical shape [55]. The Sr-ZnSe nanoparticles exhibited hexagonal shapes, as shown in Figure 6a,b. The obtained size of 36 nm provided evidence of Sr doping into the ZnSe lattice system. The particle size values are in accordance with the average crystallite size value. The particles' poly-dispersive nature came from the addition of rich Sr^{2+} cations. These results suggest that nanoparticles with larger surface areas displayed better photocatalytic activity.

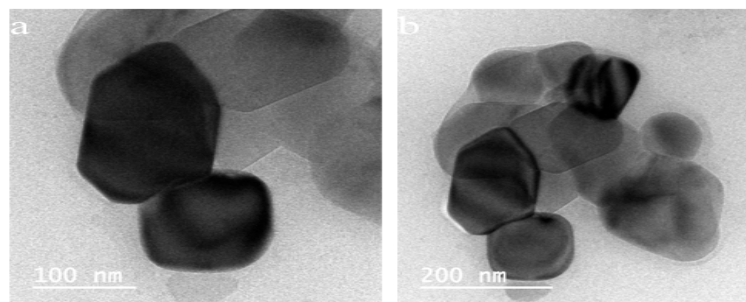


Figure 6. HR-TEM images of Sr (0.1)-doped ZnSe nanoparticles at 100 nm (a) and 200 nm (b).

3.7. XPS Analysis

The chemical compositions and valency of the synthesized Sr-doped ZnSe nanoparticle were analyzed by XPS spectra. Figure 7 represents the survey (a), Sr (b), Zn (c), Se (d), and C (e) spectrum of the Sr-doped ZnSe nanoparticles. The survey (6a) spectrum lists out the existing samples of Sr-doped ZnSe nanoparticles, such as the Sr, Zn, Se, and C elements of the samples. The core Sr metal peak spectrum was established at the binding energy of Sr-3d at 134.93eV [56].

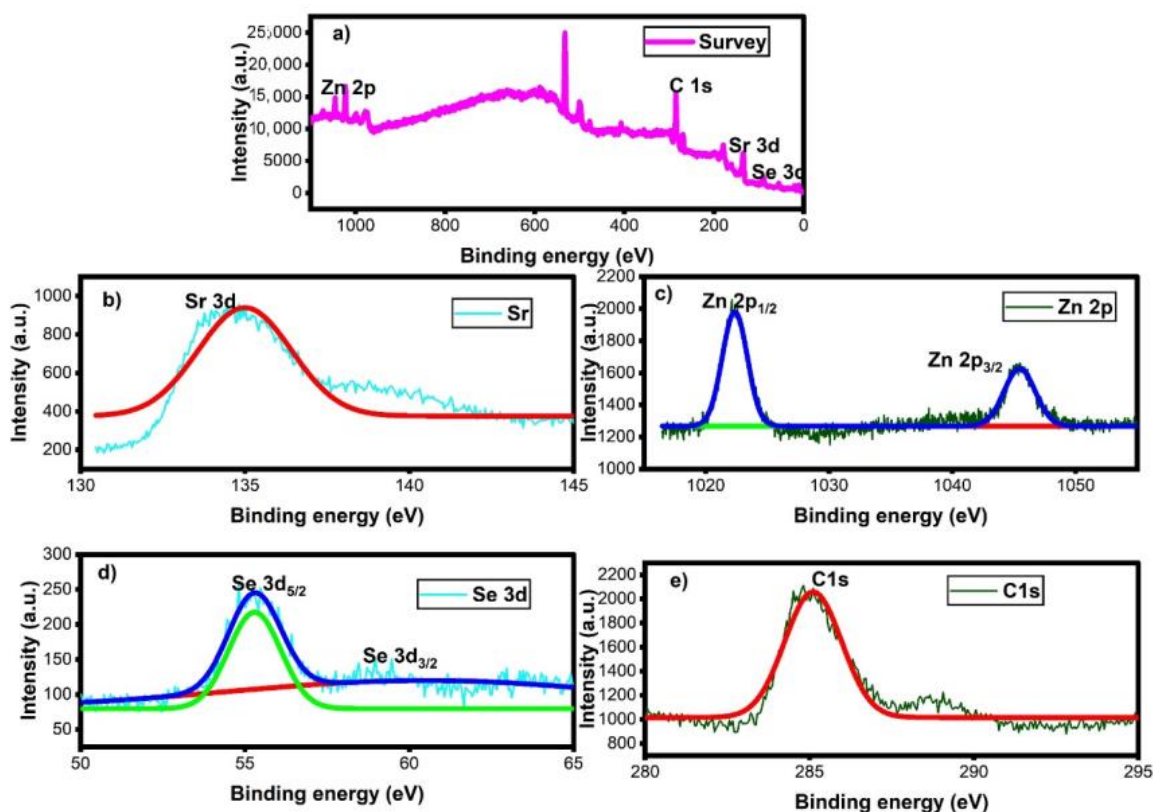


Figure 7. XPS spectra of Sr (0.1)-doped ZnSe nanoparticles; (a) wide spectrum, (b) Sr-3d spectrum, (c) Zn-2p spectrum, (d) Se-3d spectrum, and (e) C-1s spectrum.

The Sr substitution increased the electron mobility to the Zn and Se atoms. The zinc atom binding energies were 1022.50 eV and 1045.46 eV, which may represent the valency state of Zn 2p_{1/2} and Zn 2p_{3/2}, respectively [57]. As the zinc atoms shared the energies with Se and Sr atoms, the two peaks of selenium metal binding energies represent Se, which is responsible for Se 3d_{5/2} (55.34 eV) and Se 3d_{3/2} (59.01 eV). Selenium was attached to Zn atoms [58]. The combined ZnSe was decorated by Sr atoms. The Sr combination with ZnSe tremendously increased the release of ions to the target in the photocatalytic dye degradation and biological activities. The instrument peak of carbon binding energy at 285.13 eV appeared because of the calibration of the instrument. The results demonstrated that Sr depended on ZnSe nanoparticles comprising the compound of Sr, Zn, and Se. Hence, the synthesized nanoparticles could be suitable for photocatalytic applications as well as bactericidal activities.

3.8. Antibacterial Activity

Figure 8 shows the antibacterial activity of Sr-doped ZnSe nanoparticles against *E. coli* (Gram-negative) and *S. aureus* (Gram-positive) bacteria. The zone of inhibition is tabulated in Table 1 and Figure 8. The dissolution rate determined the antibacterial activity of the same nanoparticles at various concentrations. The lowest concentration produced the lowest activity compared with the 50 µL and 100 µL concentrations [45].

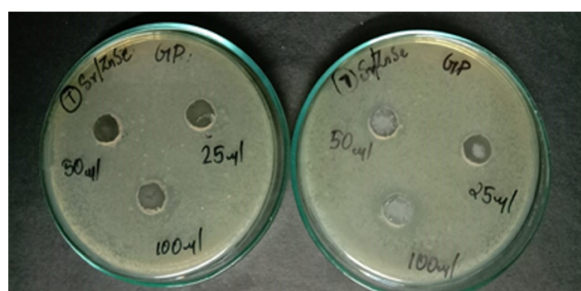


Figure 8. Antibacterial activity of Sr (0.1)-doped ZnSe nanoparticles.

Table 1. Antibacterial activity of Sr-doped ZnSe nanoparticles.

Sr-Doped ZnSe NP's	<i>B. subtilis</i>	<i>E. coli</i>
25 µL	0.5 mm	0.8 mm
50 µL	2 mm	1.5 mm
100 µL	5 mm	5.1 mm

Mechanism of Antibacterial Activity

The mechanism for antibacterial activity using Sr²⁺ doped ZnSe nanoparticles is displayed in Figure 9. The Sr-doped ZnSe nanoparticles' antibacterial activity is prominently based on reactive oxygen species (ROS). Superoxide and hydrogen peroxide were released from the reactive oxygen group. ROS affected DNA and protein production, which led to cell destruction. Both actions can destruct cellular growth and function. In addition, the nanoparticle interactions with the cell membrane could break because of their electrostatic interactions (the negatively charged cell interacts with the positively charged nanoparticles). The cell wall breakage is a starting point for the dissolved ions to enter into the bacterial system. These factors suggest that Sr-doped ZnSe nanoparticles play a robust role in bactericidal activity.

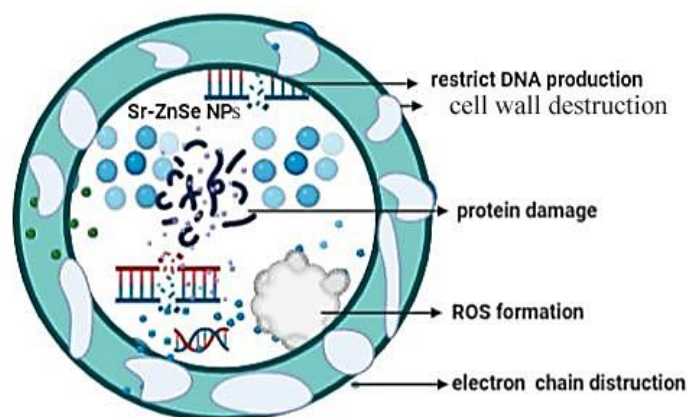


Figure 9. Antibacterial activity mechanism of Sr-doped ZnSe nanoparticles.

3.9. Photocatalytic Dye Degradation

Figure 10 demonstrates the photocatalytic dye degradation of the samples for the dye degradation activity of the MO dye solution under visible light irradiation. The pure ZnSe nanoparticles achieved a dye degradation of 75%, and the Sr-doped ZnSe nanoparticles exhibited a dye degradation of 79%, 81%, and 88% for 0.01, 0.05, and 0.1 molar ratios of Sr-doping in 120 min. The Sr-doping to the ZnSe nanoparticles increased the degradation efficiency of ZnSe and decreased the bandgap, which could induce the charge carriers. The Sr (0.1)-doped ZnSe nanoparticles expressed superior photocatalytic activity compared with the remaining two catalysts.

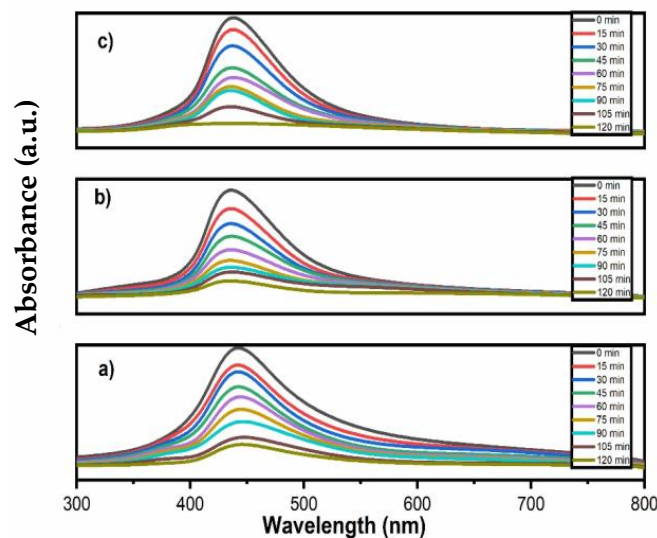


Figure 10. Photocatalyst dye degradation of (a–c) Sr-doped ZnSe nanoparticles against the MO dye spectrum.

3.10. Kinetics of Photodegradation

The dye degradation efficiency spectrum is shown in Figure 11a. It was witnessed that degradation efficiency increased with time for all Sr-doped ZnSe nanoparticle compositions. The maximum efficiency was displayed by the highest Sr content in the nanoparticles. Moreover, the degradation rate constant was calculated using Equation (3) [59]:

$$\ln \frac{C_t}{C_0} = kt \quad (3)$$

where k is the rate constant, t is the reaction time, C_t is the concentration of the dye molecules at any time interval, and C_0 is the initial concentration of the dye molecules. The rate of degradation was determined by the potential of the photocatalytic activity by plotting the

changing concentration of the dye against time, as shown in Figure 11b. The degradation rate was found in a descending order of $0.01119 (0.01) < 0.01288 (0.05) < 0.01349 (0.1) \text{ min}^{-1}$ for Sr-doping to the ZnSe nanoparticles. The Sr-doping increased the activity of the MO photodegradation. Hence, the maximum photocatalytic and bactericidal activity was displayed by the maximum dopant concentration of Sr in ZnSe nanoparticles because of its large surface area, reduced bandgap, nano size, and improved electronic properties. Therefore, the Sr-doped ZnSe nanoparticles could have great applicability with respect to environmental and biological remediations.

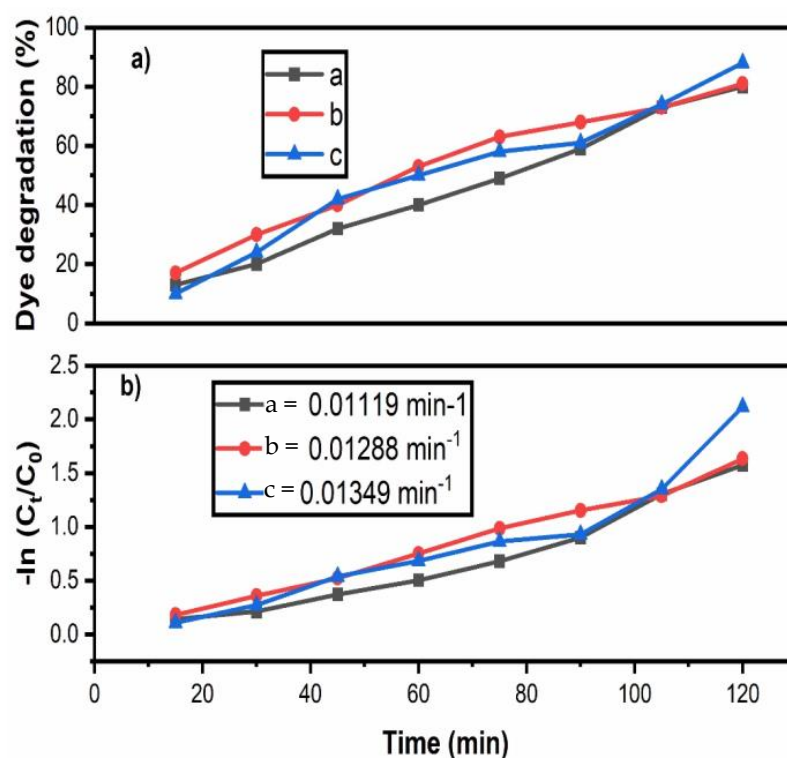
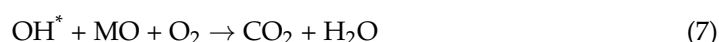


Figure 11. Photocatalytic dye degradation efficiency (a) percentage and (b) pseudo-first-order kinetics of the Sr/ZnSe nanoparticles.

Mechanism of Photodegradation

The detailed photocatalytic dye degradation mechanism is expressed in Equations (4)–(9). Figure 12 also illustrates the mechanism of photocatalytic degradation of methyl orange. The light irradiation induced the electron–hole pair recombination in the process of oxidation and reduction. It could produce OH radicals from the oxygen surface. The photogenerated free radicals and superoxide radicals strongly degraded the organic dye molecules and produced noxious compounds in the environment.



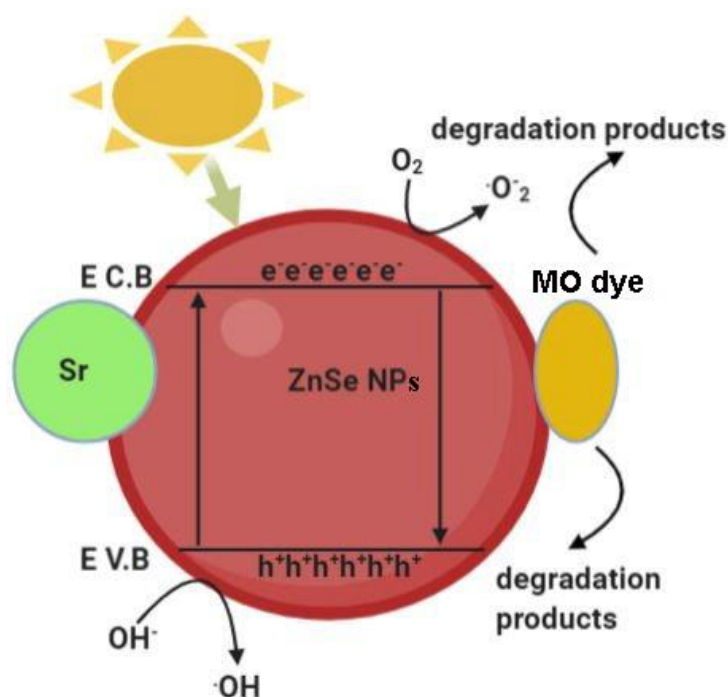


Figure 12. Photocatalytic dye degradation mechanism of the Sr-doped ZnSe nanoparticles.

4. Conclusions

Sr-doped ZnSe nanoparticles, exhibiting three different molar ratios of Sr, i.e., 0.01, 0.05, and 0.1, were prepared via the cost-effective co-precipitation method. The average crystallite sizes in nanodimensions indicated the synthesis of nanoparticles. The FTIR spectra suggested the formation of metallic bonds. UV-DRS displayed the reduced bandgap with the incorporation of Sr dopant. The FE-SEM and HR-TEM images corresponded to the XRD analysis such that the hexagonal crystals obtained also possessed a nano size. Lattice reorientation was analyzed using XPS analysis. Sr^{2+} doping (0.01–0.1) to the ZnSe nanoparticles revealed enhanced structural, optical, and morphological properties. The Sr^{2+} -doped ZnSe nanoparticles showed boosted antibacterial activity toward both bacterial strains. The photocatalytic dye degradation of MO dye using Sr^{2+} -doped ZnSe nanoparticles achieved the degradation efficiency in a concentration-dependent manner, i.e., $79\% < 81\% < 88\%$ for 0.01, 0.05, and 0.1 molar ratios, respectively. The dye degradation and their pseudo-first-order kinetics distinctly advocated that the Sr (0.10)-doped ZnSe nanoparticles were superior to the other compositions. Thus, Sr-doped ZnSe nanoparticles could act as an efficient photocatalyst for wastewater treatment and a suitable bactericidal agent in biomedical applications.

Author Contributions: V.B. and S.A. designed the research scheme and carried out the experimental work. A.A. and V.B. wrote the manuscript. S.L.R., F.A.A.A., and A.A. interpreted the experimental and characterization data. M.D.A. and M.S. All authors have read and agreed to the published version of the manuscript.

Funding: This work was funded by the Researchers Supporting Project Number (RSP-2021/267) King Saud University, Riyadh, Saudi Arabia.

Informed Consent Statement: Not applicable.

Data Availability Statement: Not applicable.

Conflicts of Interest: The authors declare no conflict of interest related to this research.

References

1. Aeenjan, F.; Javanbakht, V. Methylene blue removal from aqueous solution by magnetic clinoptilolite/chitosan/EDTA nanocomposite. *Res. Chem. Intermed.* **2017**, *44*, 1459–1483. [[CrossRef](#)]
2. Pandey, S.; Fosso-Kankeu, E.; Redelinguys, J.; Kim, J.; Kang, M. Implication of biofilms in the sustainability of acid mine drainage and metal dispersion near coal tailings. *Sci. Total Environ.* **2021**, *788*, 147851. [[CrossRef](#)]
3. Gupta, V.K.; Jain, R.; Nayak, A.; Agarwal, S.; Shrivastava, M. Removal of the hazardous dye—Tartrazine by photodegradation on titanium dioxide surface. *Mater. Sci. Eng. C* **2011**, *31*, 1062–1067. [[CrossRef](#)]
4. Erfani, M.; Javanbakht, V. Methylene Blue removal from aqueous solution by a biocomposite synthesized from sodium alginate and wastes of oil extraction from almond peanut. *Int. J. Biol. Macromol.* **2018**, *114*, 244–255. [[CrossRef](#)]
5. Mittal, A.; Mittal, J.; Malviya, A.; Gupta, V. Removal and recovery of Chrysoidine Y from aqueous solutions by waste materials. *J. Colloid Interface Sci.* **2010**, *344*, 497–507. [[CrossRef](#)]
6. Yagub, M.T.; Sen, T.K.; Afroze, S.; Ang, H. Dye and its removal from aqueous solution by adsorption: A review. *Adv. Colloid Interface Sci.* **2014**, *209*, 172–184. [[CrossRef](#)]
7. Bibi, S.; Ahmad, A.; Anjum, M.A.R.; Haleem, A.; Siddiq, M.; Shah, S.S.; Al Kahtani, A. Photocatalytic degradation of malachite green and methylene blue over reduced graphene oxide (rGO) based metal oxides (rGO-Fe₃O₄/TiO₂) nanocomposite under UV-visible light irradiation. *J. Environ. Chem. Eng.* **2021**, *9*, 105580. [[CrossRef](#)]
8. Pandey, S.; Do, J.Y.; Kim, J.; Kang, M. Fast and highly efficient catalytic degradation of dyes using κ-carrageenan stabilized silver nanoparticles nanocatalyst. *Carbohydr. Polym.* **2020**, *230*, 115597. [[CrossRef](#)]
9. Pandey, S.; Fosso-Kankeu, E.; Spiro, M.; Waanders, F.; Kumar, N.; Ray, S.; Kim, J.; Kang, M. Equilibrium, kinetic, and thermodynamic studies of lead ion adsorption from mine wastewater onto MoS₂-clinoptilolite composite. *Mater. Today Chem.* **2020**, *18*, 100376. [[CrossRef](#)]
10. Aravind, M.; Ahmad, A.; Ahmad, I.; Amalanathan, M.; Naseem, K.; Mary, S.M.M.; Parvathiraja, C.; Hussain, S.; Algarni, T.S.; Pervaiz, M.; et al. Critical green routing synthesis of silver NPs using jasmine flower extract for biological activities and photocatalytic degradation of methylene blue. *J. Environ. Chem. Eng.* **2020**, *9*, 104877. [[CrossRef](#)]
11. Ahmad, A.; Jini, D.; Aravind, M.; Parvathiraja, C.; Ali, R.; Kiyani, M.Z.; Alothman, A. A novel study on synthesis of egg shell based activated carbon for degradation of methylene blue via photocatalysis. *Arab. J. Chem.* **2020**, *13*, 8717–8722. [[CrossRef](#)]
12. Younas, U.; Hassan, S.; Ali, F.; Hassan, F.; Saeed, Z.; Pervaiz, M.; Khan, S.; Jannat, F.; Bibi, S.; Sadiqa, A.; et al. Radical Scavenging and Catalytic Activity of Fe-Cu Bimetallic Nanoparticles Synthesized from *Ixora finlaysoniana* Extract. *Coatings* **2021**, *11*, 813. [[CrossRef](#)]
13. Chong, M.N.; Jin, B.; Chow, C.W.K.; Saint, C. Recent developments in photocatalytic water treatment technology: A review. *Water Res.* **2010**, *44*, 2997–3027. [[CrossRef](#)]
14. Chakrabarti, S.; Chaudhuri, B.; Bhattacharjee, S.; Das, P.; Dutta, B.K. Degradation mechanism and kinetic model for photocatalytic oxidation of PVC-ZnO composite film in presence of a sensitizing dye and UV radiation. *J. Hazard. Mater.* **2008**, *154*, 230–236. [[CrossRef](#)]
15. Lan, Y.; Lu, Y.; Ren, Z. Mini review on photocatalysis of titanium dioxide nanoparticles and their solar applications. *Nano Energy* **2013**, *2*, 1031–1045. [[CrossRef](#)]
16. Ong, C.B.; Ng, L.Y.; Mohammad, A.W. A review of ZnO nanoparticles as solar photocatalysts: Synthesis, mechanisms and applications. *Renew. Sustain. Energy Rev.* **2018**, *81*, 536–551. [[CrossRef](#)]
17. Mishra, M.K.; Singh, N.; Pandey, V.; Haque, F.Z. Synthesis of SnO₂ Nanoparticles and Its Application in Sensing Ammonia Gas Through Photoluminescence. *J. Adv. Phys.* **2016**, *5*, 8–12. [[CrossRef](#)]
18. Cheng, L.; Xiang, Q.; Liao, Y.; Zhang, H. CdS-based photocatalysts. *Energy Environ. Sci.* **2018**, *11*, 1362–1391. [[CrossRef](#)]
19. Boulkroune, R.; Sebaï, M.; Messai, Y.; Bourzami, R.; Schmutz, M.; Blanck, C.; Halimi, O.; Boudine, B. Hydrothermal synthesis of strontium-doped ZnS nanoparticles: Structural, electronic and photocatalytic investigations. *Bull. Mater. Sci.* **2019**, *42*, 223. [[CrossRef](#)]
20. Dai, S.; Wang, B.; Li, W.; Wang, L.; Song, X.; Guo, C.; Li, Y.; Liu, F.; Zhu, F.; Wang, Q.; et al. Systemic application of 3-methyladenine markedly inhibited atherosclerotic lesion in ApoE^{-/-} mice by modulating autophagy, foam cell formation and immune-negative molecules. *Cell Death Dis.* **2016**, *7*, e2498. [[CrossRef](#)]
21. Patel, B.; Rath, S.; Sarangi, S.N.; Sahu, S. HgS nanoparticles: Structure and optical properties. *Appl. Phys. A* **2007**, *86*, 447–450. [[CrossRef](#)]
22. Naseem, K.; Rehman, M.Z.U.; Ahmad, A.; Dubal, D.; Algarni, T.S. Plant Extract Induced Biogenic Preparation of Silver Nanoparticles and Their Potential as Catalyst for Degradation of Toxic Dyes. *Coatings* **2020**, *10*, 1235. [[CrossRef](#)]
23. Fallah, Z.; Zare, E.N.; Ghomi, M.; Ahmadijokani, F.; Amini, M.; Tajbakhsh, M.; Arjmand, M.; Sharma, G.; Ali, H.; Ahmad, A.; et al. Toxicity and remediation of pharmaceuticals and pesticides using metal oxides and carbon nanomaterials. *Chemosphere* **2021**, *275*, 130055. [[CrossRef](#)]
24. Hu, X.-L.; Shang, Y.; Yan, K.-C.; Sedgwick, A.C.; Gan, H.-Q.; Chen, G.-R.; He, X.-P.; James, T.D.; Chen, D. Low-dimensional nanomaterials for antibacterial applications. *J. Mater. Chem. B* **2021**, *9*, 3640–3661. [[CrossRef](#)]
25. Menazea, A.; Ahmed, M. Synthesis and antibacterial activity of graphene oxide decorated by silver and copper oxide nanoparticles. *J. Mol. Struct.* **2020**, *1218*, 128536. [[CrossRef](#)]

26. Krishna, A.G.R.; Espenti, C.S.; Reddy, Y.V.R.; Obbu, A.; Satyanarayana, M.V. Green Synthesis of Silver Nanoparticles by Using *Sansevieria Roxburghiana*, Their Characterization and Antibacterial Activity. *J. Inorg. Organomet. Polym. Mater.* **2020**, *30*, 4155–4159. [[CrossRef](#)]
27. Varghese, B.; Kurian, M.; Krishna, S.; Athira, T. Biochemical synthesis of copper nanoparticles using *Zingiber officinalis* and *Curcuma longa*: Characterization and antibacterial activity study. *Mater. Today Proc.* **2020**, *25*, 302–306. [[CrossRef](#)]
28. Agarwal, H.; Menon, S.; Shanmugam, V.K. Functionalization of zinc oxide nanoparticles using *Mucuna pruriens* and its antibacterial activity. *Surf. Interfaces* **2020**, *19*, 100521. [[CrossRef](#)]
29. Rajbongshi, H.; Kalita, D. Morphology-Dependent Photocatalytic Degradation of Organic Pollutant and Antibacterial Activity with CdS Nanostructures. *J. Nanosci. Nanotechnol.* **2020**, *20*, 5885–5895. [[CrossRef](#)] [[PubMed](#)]
30. Yang, Y.; Wu, Z.; Yang, R.; Li, Y.; Liu, X.; Zhang, L.; Yu, B. Insights into the mechanism of enhanced photocatalytic dye degradation and antibacterial activity over ternary ZnO/ZnSe/MoSe₂ photocatalysts under visible light irradiation. *Appl. Surf. Sci.* **2021**, *539*, 148220. [[CrossRef](#)]
31. Beena, V.; Ajitha, S.; Rayar, S.L.; Parvathiraja, C.; Kannan, K.; Palani, G. Enhanced Photocatalytic and Antibacterial Activities of ZnSe Nanoparticles. *J. Inorg. Organomet. Polym. Mater.* **2021**, *4*, 1–12.
32. Gao, Z.; Chen, S.; Li, R.; Lou, Z.; Han, W.; Jiang, K.; Qu, F.; Shen, G. An artificial olfactory system with sensing, memory and self-protection capabilities. *Nano Energy* **2021**, *86*, 106078. [[CrossRef](#)]
33. Kageshima, Y.; Gomyo, Y.; Matsuoka, H.; Inuzuka, H.; Suzuki, H.; Abe, R.; Teshima, K.; Domen, K.; Nishikiori, H. Z-Scheme Overall Water Splitting Using Zn_xCd_{1-x}Se Particles Coated with Metal Cyanoferrates as Hydrogen Evolution Photocatalysts. *ACS Catal.* **2021**, *11*, 8004–8014. [[CrossRef](#)]
34. Liu, Y.; Bai, G.; Lyu, Y.; Hua, Y.; Ye, R.; Zhang, J.; Chen, L.; Xu, S.; Hao, J. Ultrabroadband Tuning and Fine Structure of Emission Spectra in Lanthanide Er-Doped ZnSe Nanosheets for Display and Temperature Sensing. *ACS Nano* **2020**, *14*, 16003–16012. [[CrossRef](#)]
35. Khan, M.S.; Shi, L.; Zou, B. Impact of vacancy defects on optoelectronic and magnetic properties of Mn-doped ZnSe. *Comput. Mater. Sci.* **2020**, *174*, 109493. [[CrossRef](#)]
36. Sharma, V.; Mehata, M.S. Synthesis of photoactivated highly fluorescent Mn²⁺-doped ZnSe quantum dots as effective lead sensor in drinking water. *Mater. Res. Bull.* **2021**, *134*, 111121. [[CrossRef](#)]
37. Feng, K.; Xue, W.; Hu, X.; Fan, J.; Liu, E. Z-scheme CdSe/ZnSe heterojunction for efficient photocatalytic hydrogen evolution. *Colloids Surf. A Physicochem. Eng. Asp.* **2021**, *622*, 126633. [[CrossRef](#)]
38. Tian, P.; Tang, T.; Zhang, J.; Lin, S.; Huang, G.; Zeng, J.; Kong, Z.; Wang, H.; Xi, J.; Ji, Z. High photocatalytic and photoelectrochemical performance of a novel 0D/2D heterojunction photocatalyst constructed by ZnSe nanoparticles and MoSe₂ nanoflowers. *Ceram. Int.* **2020**, *46*, 13651–13659. [[CrossRef](#)]
39. Kasture, M.B.; Patel, P.; Prabhune, A.A.; Ramana, C.V.; Kulkarni, A.A.; Prasad, B.L.V. Synthesis of silver nanoparticles by sophorolipids: Effect of temperature and sophorolipid structure on the size of particles. *J. Chem. Sci.* **2008**, *120*, 515–520. [[CrossRef](#)]
40. Fayaz, A.M.; Balaji, K.; Kalaichelvan, P.; Venkatesan, R. Fungal based synthesis of silver nanoparticles—An effect of temperature on the size of particles. *Colloids Surf. B Biointerfaces* **2009**, *74*, 123–126. [[CrossRef](#)]
41. Lee, G. Preparation of silver nanorods through the control of temperature and pH of reaction medium. *Mater. Chem. Phys.* **2004**, *84*, 197–204. [[CrossRef](#)]
42. Wang, Q.; Liu, F.T.; Jiang, Q.H.; Chen, X.X.; Wang, D.Z. Luminescence of Cu²⁺-Doped ZnSe Quantum Dots with Different Parameters. *Adv. Mater. Res.* **2010**, *148–149*, 1268–1272.
43. Thor, H.Y.; Teow, Y.H.; Ho, K.C. Synthesis and characterization of 2-mercaptoethanol-capped manganese-doped zinc sulfide quantum dots-embedded molecularly-imprinted membranes. *Part. Sci. Technol.* **2021**, 1–8. [[CrossRef](#)]
44. Ganjali, M.R.; Al-Naqshabandi, M.A.; Larjani, B.; Badiei, A.; Vatanpour, V.; Rajabi, H.R.; Rezaia, H.; Paziresh, S.; Mahmodi, G.; Kim, S.-J.; et al. Improvement of dye and protein filtration efficiency using modified PES membrane with 2-mercaptoethanol capped zinc sulfide quantum dots. *Chem. Eng. Res. Des.* **2021**, *168*, 109–121. [[CrossRef](#)]
45. Yarahmadi, M.; Maleki-Ghaleh, H.; Mehr, M.E.; Dargahi, Z.; Rasouli, F.; Siadati, M.H. Synthesis and characterization of Sr-doped ZnO nanoparticles for photocatalytic applications. *J. Alloy Compd.* **2021**, *853*, 157000. [[CrossRef](#)]
46. Khan, S.; Shah, S.; Anjum, M.; Khan, M.; Janjua, N. Electro-Oxidation of Ammonia over Copper Oxide Impregnated γ -Al₂O₃ Nanocatalysts. *Coatings* **2021**, *11*, 313. [[CrossRef](#)]
47. Ban, Y.; Prates, L.L.; Feng, X.; Khan, N.A.; Yu, P. Novel Use of Ultra-Resolution Synchrotron Vibrational Microspectroscopy (SR-FT/vIMS) to Assess Carinata and Canola oilseed tissues within Cellular and Subcellular Dimensions. *Spectrochim. Acta Part A Mol. Biomol. Spectrosc.* **2021**, *246*, 118934. [[CrossRef](#)]
48. Hack, J.H.; Dombrowski, J.P.; Ma, X.; Chen, Y.; Lewis, N.H.C.; Carpenter, W.B.; Li, C.; Voth, G.A.; Kung, H.H.; Tokmakoff, A. Structural Characterization of Protonated Water Clusters Confined in HZSM-5 Zeolites. *J. Am. Chem. Soc.* **2021**, *143*, 10203–10213. [[CrossRef](#)]
49. Ali, R.H.; Ageorges, H.; Nasr, S.; Ben Salem, E. Zinc and strontium co-substituted hydroxyfluorapatite: Synthesis, sintering and mechanical properties. *Mater. Res. Bull.* **2019**, *112*, 84–94. [[CrossRef](#)]
50. Dewangan, P.; Bisen, D.P.; Brahme, N.; Sharma, S.; Tamrakar, R.K.; Sahu, I.P. Thermoluminescence glow curve for UV induced Sr₃MgSi₂O₈ phosphor with its structural characterization. *J. Mater. Sci. Mater. Electron.* **2018**, *30*, 771–777. [[CrossRef](#)]

51. Shavel, A.; Gaponik, N.; Eychmüller, A. Efficient UV-Blue Photoluminescing Thiol-Stabilized Water-Soluble Alloyed ZnSe(S) Nanocrystals. *J. Phys. Chem. B* **2004**, *108*, 5905–5908. [[CrossRef](#)]
52. Quinlan, F.T.; Kuther, J.; Tremel, W.; Knoll, W.; Risbud, S.; Stroeve, P. Reverse Micelle Synthesis and Characterization of ZnSe Nanoparticles. *Langmuir* **2000**, *16*, 4049–4051. [[CrossRef](#)]
53. Laajalehto, K.; Kartio, I.; Suoninen, E. XPS and SR-XPS techniques applied to sulphide mineral surfaces. *Int. J. Miner. Process.* **1997**, *51*, 163–170. [[CrossRef](#)]
54. Calzaferri, G.; Imhof, R. In situ attenuated total reflection FTIR investigations of H₂O, HSiCl₃ and Co₂(CO)₈ on ZnSe in the range 600–4000 cm⁻¹. *Spectrochim. Acta Part A Mol. Biomol. Spectrosc.* **1996**, *52*, 23–28. [[CrossRef](#)]
55. Kotsis, K.; Staemmler, V. Ab initio calculations of the O1s XPS spectra of ZnO and Zn oxo compounds. *Phys. Chem. Chem. Phys.* **2006**, *8*, 1490–1498. [[CrossRef](#)]
56. Canava, B.; Vigneron, J.; Etcheberry, A.; Guillemoles, J.-F.; Lincot, D. High resolution XPS studies of Se chemistry of a Cu(In, Ga)Se₂ surface. *Appl. Surf. Sci.* **2002**, *202*, 8–14. [[CrossRef](#)]
57. Yao, T.; Zhao, Q.; Qiao, Z.; Peng, F.; Wang, H.; Yu, H.; Chi, C.; Yang, J. Chemical Synthesis, Structural Characterization, Optical Properties, and Photocatalytic Activity of Ultrathin ZnSe Nanorods. *Chem. Eur. J.* **2011**, *17*, 8663–8670. [[CrossRef](#)]
58. Lin, X.; Huang, F.; Wang, W.; Wang, Y.; Xia, Y.; Shi, J. Photocatalytic activities of M₂Sb₂O₇ (M=Ca, Sr) for degrading methyl orange. *Appl. Catal. A Gen.* **2006**, *313*, 218–223. [[CrossRef](#)]
59. Ahmad, I.; Jamal, M.; Iftikhar, M.; Ahmad, A.; Hussain, S.; Asghar, H.; Saeed, M.; Yousaf, A.; Karri, R.; Al-Kadhi, N.; et al. Lanthanum-Zinc Binary Oxide Nanocomposite with Promising Heterogeneous Catalysis Performance for the Active Conversion of 4-Nitrophenol into 4-Aminophenol. *Coatings* **2021**, *11*, 537. [[CrossRef](#)]